Available online at www.sciencedirect.com
ScienceDirect
Trans. Nonferrous Met. Soc. China 35(2025) 1440−1455
Transactions of Nonferrous Metals Society of China
www.tnmsc.cn

Mechanical properties and corrosion behavior of hetero-structured lean Mg−1Bi−0.5Sn−0.5In alloy

Hong-wei XU[1], Wen-ting XU[1], Wei-li CHENG[1,2], Jian LI[2],
Li-fei WANG[1], Hui YU[3], Jin-hui WANG[2], Hua HOU[4], Kwang Seon SHIN[5]

1. School of Materials Science and Engineering, Taiyuan University of Technology, Taiyuan 030024, China;
2. The Open Project of Salt Lake Chemical Engineering Research Complex, Qinghai University, Xining 810016, China;
3. School of Materials Science and Engineering, Hebei University of Technology, Tianjin 300132, China;
4. School of Materials Science and Engineering, North University of China, Taiyuan 030051, China;
5. Magnesium Technology Innovation Center, Department of Materials Science and Engineering, Seoul National University, Seoul-08826, Korea

Received 31 August 2023; accepted 25 March 2024

Abstract: The microstructural characterization, corrosion behavior and tensile properties of the extruded lean Mg−1Bi−0.5Sn−0.5In (wt.%) alloy were investigated through scanning electron microscopy (SEM), electron backscatter diffraction (EBSD), X-ray photoelectron spectroscopy (XPS), electrochemical measurements and tensile tests. The results reveal that a microstructure consisting of dynamically recrystallized and deformed grains is obtained. Notably, the investigated alloy exhibits excellent strength−ductility synergy, with tensile yield strength (TYS), ultimate tensile strength (UTS) and elongation (EL) of 254.8 MPa, 315.4 MPa, and 25.3%, respectively. Furthermore, in 3.5 wt.% NaCl solution, with the increase of immersion time, the dominant corrosion mechanism of the studied alloy transforms from pitting corrosion to filiform corrosion. After the immersion for 24 h, a composite oxide film (SnO_2−Bi_2O_3−In_2O_3) is formed, which delays the corrosion process, and the corrosion rate (P_H=1.53 mm/a) is finally stabilized.
Key words: Mg alloy; extrusion; corrosion behavior; tensile properties; strengthening mechanism

1 Introduction

As the lightest metal structure materials, Mg and Mg alloys have attracted considerable attention due to their low density and high specific strength [1−3]. Nevertheless, the inferior synergy between mechanical properties and corrosion resistance has been an obstacle to impede their widespread industrial applications [4,5]. Lean Mg−Bi-based alloys with thermally stable Mg_3Bi_2 phases have attracted increasing attention in recent years owing to their outstanding extrudability and ductility [6−9]. The dynamic precipitation of the nanoscale Mg_3Bi_2 phase during the extrusion process can inhibit grain growth effectively, leading to a fine-grained structure that improves the strength and plasticity of Mg alloys [6,10,11]. Nevertheless, the presence of the Mg_3Bi_2 phase may accelerate the micro-galvanic corrosion. Moreover, an efficient protective film is difficult to be formed on their surface [12].

Alloying is an important means to improve the comprehensive performance of lean Mg−Bi alloys [10,11]. The selected alloying elements should provide a suitable solid solubility without

Corresponding author: Wei-li CHENG, Tel: +86-18636612588, E-mail: chengweili7@126.com;
Jian LI, Tel: +86-13389710640, E-mail: ljnjx@sohu.com
https://doi.org/10.1016/S1003-6326(24)66759-2

introduction of precipitated phase and a nobler corrosion potential than Mg. Sn has a higher hydrogen evolution overpotential [13] than Mg and relatively high solubility in Mg matrix, thereby hardly producing a second phase in the case of micro alloying with Sn. SONG [14] found that Sn alloying reduces the sensitivity of AM70 alloy to localized corrosion attacks significantly owing to the inhibition of hydrogen precipitation. Similarly, CHEN et al [15] reported that the addition of Sn could reduce the cathodic current density, thus slowing down the corrosion process of the Mg−6Zn−2Al alloy.

Furthermore, WANG et al [16] reported that In alloying delayed the cathodic reaction, thereby improving the resistance to corrosion of the Mg−5Sn alloy. Additionally, YIN et al [17] reported that the double protective film formed in Mg−In alloys could inhibit corrosion propagation significantly. The above analysis suggests that the Sn/In micro-alloying may be an effective strategy to further improve the corrosion resistance of the Mg alloys. Meanwhile, the Sn and In alloying can induce solid solution strengthening, which improves the mechanical performance of the alloy. Therefore, it is expected that the microalloying of Sn and In can improve the corrosion resistance and mechanical properties of Mg−Bi based alloys at the same time.

In addition to micro-alloying, tailoring of the grain structure, especially the heterogeneous grain structure, plays an essential role in enhancing the strength and ductility simultaneously. For example, ZHANG et al [18] fabricated Mg−0.8Zn−0.2Zr alloy with a bimodal microstructure using routine extrusion at a low temperature (250 °C). An excellent combination of strength and ductility was achieved, which was ascribed to the presence of ultrafine recrystallized grains and a small portion of strong textured deformed grains having sufficient dislocation storage ability. Similarly, WU et al [19] indicated that an excellent strength−plasticity synergy could be achieved in pure Ti with a heterogeneous lamellar structure, which is related to the back stress and dislocation hardening. However, a large number of studies have been focused on the effect of heterogeneous grain structure on mechanical properties, and the effect on the corrosion resistance has remained inconclusive.

Therefore, the main purpose of this study is to study the synergistic effects of heterogeneous grain structures on the mechanical properties and corrosion behavior of the extruded Mg−1Bi−0.5Sn−0.5In (wt.%) alloy and to establish the underlying strengthening and corrosion mechanisms in terms of grain structure, second phase particles and dislocation density.

2 Experimental

2.1 Material preparation

A Mg−1Bi−0.5Sn−0.5In cast ingot was fabricated by melting pure Mg, Bi, Sn, and In (provided by Zhongnuo Advanced Materials Technology, Beijing, China) in a resistance furnace at 750 °C in a mixed atmosphere of CO_2 and SF_6 to prevent oxidation. The actual composition was measured as Mg−1.03Bi−0.49Sn−0.53In (wt.%) through inductively coupled plasma mass spectrometry (ICP-MS). The ingot was maintained at 320 °C for 1 h and then 500 °C for 5 h for homogenization, prior to cooling in water. Then, the ingot was aged at 200 °C for 60 h prior to extrusion to achieve peak hardness. Subsequently, the ingot was extruded using an extrusion ratio of 16:1 at 225 °C with an extrusion speed of 30 mm/min to obtain extrusion bar with a diameter of 10 mm.

2.2 Microstructural characterization

The microstructure of the extruded bar was observed by X-ray diffraction (XRD, Rigaku Ultima IV), field-emission scanning electron microscopy (SEM, TESCAN MIRA LMS) with energy dispersive spectrometry (EDS, Xplore), and electron backscatter diffraction (EBSD, JEOL JSM−7000F). The specimens used for SEM observation were ground, polished, and then etched with an acetic-picral solution. The operation voltages for SEM and EDS characterization were 3 and 15 kV, respectively. The EBSD results were managed by HKL channel 5 software. The detailed EBSD sample production procedure was outlined in our previous study [20]. The 3D corrosion morphology of the sample was obtained using laser scanning confocal microscopy (LSCM, KEYENCE VK−X150).

2.3 Tensile property tests

Tensile test samples with a size of 18 mm (length) × 4 mm (width) × 2 mm (thickness) were

cut along the extrusion direction (ED) of the alloy bar, and at least three samples were examined. The tensile tests were conducted on an Instron 5982 testing machine with a strain rate of 1×10^{-3} s^{-1} at room temperature. The microstructure evolution of the fractured sample was observed by SEM and EBSD.

2.4 Electrochemical tests

Electrochemical tests were carried out at (25±1) °C in 3.5 wt.% NaCl solution using a CS350H (CorrTest, Wuhan, China). A three-electrode testing system was established, during which the specimen was the working electrode (exposure area: 1 cm^2), a platinum mesh was regarded as the counter electrode, and a saturated calomel electrode (SCE) was set as the reference electrode. Various samples were immersed in the solution for 30 min prior to the polarization tests to achieve a relatively steady open-circuit potential (OCP). The polarization tests were conducted in the range of ±300 mV vs OCP with a scan rate of 0.5 mV/s. The corrosion rate (P_i) was performed by the standard formula of ASTM G59—97 as follows:

$$P_i=\frac{3.27\times10^{-3}\cdot J_{corr}\cdot W_E}{\rho\cdot S} \quad (1)$$

where W_E is the equivalent mass (12.15 g) for Mg, ρ is the density (1.756 g/cm^3) of the studied alloy, S is the corroded surface (1 cm^2) of the alloys, and J_{corr} is the corrosion density. Therefore, it could be simplified to P_i=22.63J_{corr}. Electrochemical impedance spectroscopy (EIS) was carried out in a sinusoidal AC wave of ±10 mV amplitude at the OCP with the frequency range from 100 kHz to 0.01 Hz. The results were further characterized using the ZsimpWin software. Three parallel polarization curves and EIS measurements were performed using the same test parameters to ensure accuracy.

2.5 Immersion tests and surface analysis

The hydrogen tests were conducted in the solution of 3.5 wt.% NaCl at 25 °C. The samples were mechanically ground with 800$^{\#}$–4000$^{\#}$ sandpapers and polished with the testing plane along the ED−transverse direction (TD). The corrosion rate (P_H, mm/a) could be calculated from the hydrogen evolution rate (V_H, mL/(cm^2·d)) via the following equation [21]:

$$P_H=3.96V_H/\rho \quad (2)$$

Therefore, it could be simplified to P_H=2.255V_H. The surface morphologies were investigated by SEM after immersion at different time to reveal corrosion evolution. In order to observe the morphology of de-corroded products, the surface corrosion products were cleared with chromic acid (200 g/L CrO_3 + 10 g/L $AgNO_3$) for 10 min. After immersion for 4 and 24 h, the corrosion products were collected and their chemical composition was analyzed by X-ray photoelectron spectroscopy (XPS; Thermo Scientific K$_\alpha$).

2.6 Density functional theory calculation

The Vienna Ab-initio Simulation Package (VASP) and van der Waals (DFT-D3) corrections were used to perform first-principles density-functional theory (DFT) calculations. The binding energies of an additional Mg atom to the Mg (002), Mg (100), and Mg (101) surfaces, as well as the surface layer atom removal energies of the Mg (002), Mg (100), and Mg (101) substrates, were calculated using the following formula:

$$E_S=E_{hkl-1}+E_{Mg1}-E_{hkl} \quad (3)$$

where E_{hkl-1}, E_{hkl}, and E_{Mg1} denote the overall energy of Mg surface with an adsorbed Mg atom (removal energy is the total energy of Mg with a complete surface), energy of the Mg surfaces with different crystal planes, and energy of a Mg atom, respectively. The crystal structure of Mg was modeled in a 3 × 3 × 1 supercell with a 15 Å vacuum layer. The Mg atoms were placed in a framework with the same lattice parameters as Mg (*hkl*) to prevent interference from periodic calculations. The Mg atoms were fixed at specific positions on the Mg (*hkl*) surfaces, with the bottom two layers fixed and the top layer relaxed. The cutoff energy for the calculations was established at 400 eV, while the tolerance for geometry optimization convergence was set as 1.0×10^{-5} eV per atom. The maximum force and the displacement were set to be 2.0×10^{-2} eV/Å and 1.0×10^{-3} Å, correspondingly.

3 Results

3.1 Microstructural characterization

Figure 1 presents the XRD pattern of the investigated alloy. In addition to the peaks

corresponding to α-Mg, some peaks can also be observed. Based on the analyses of the powder diffraction files (PDF) card (04-0464), these peaks are related to the Mg_3Bi_2 phase. Furthermore, several fine precipitates are observed in the SEM images, as illustrated in Fig. 2. Based on the EDS together with the XRD results, these precipitates can be identified as Mg_3Bi_2 phase rich in Sn/In.

Figure 3 depicts the EBSD results of the studied alloy. In Fig. 3(a), the high-angle grain boundaries (HAGB, >15°) and low-angle grain boundaries (LAGB, 2°−15°) are indicated by the black and gray lines, respectively. The grain size statistics demonstrate a bimodal distribution that consists of equiaxed grains (FGs) of <6 μm and

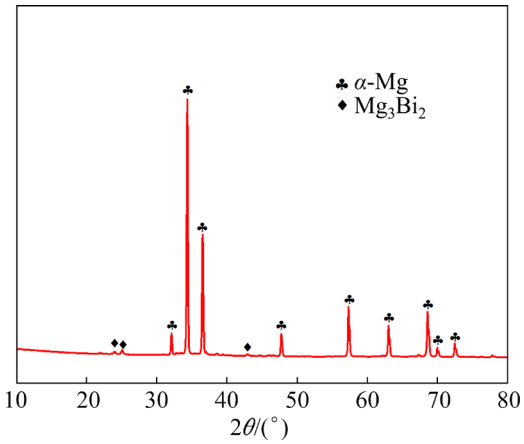

Fig. 1 XRD pattern of extruded Mg−1Bi−0.5Sn−0.5In alloy

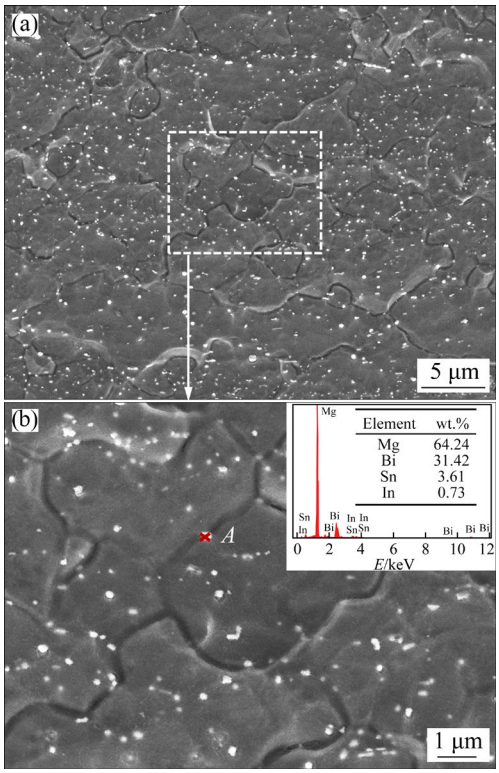

Fig. 2 SEM images with EDS results of extruded Mg−1Bi−0.5Sn−0.5In alloy

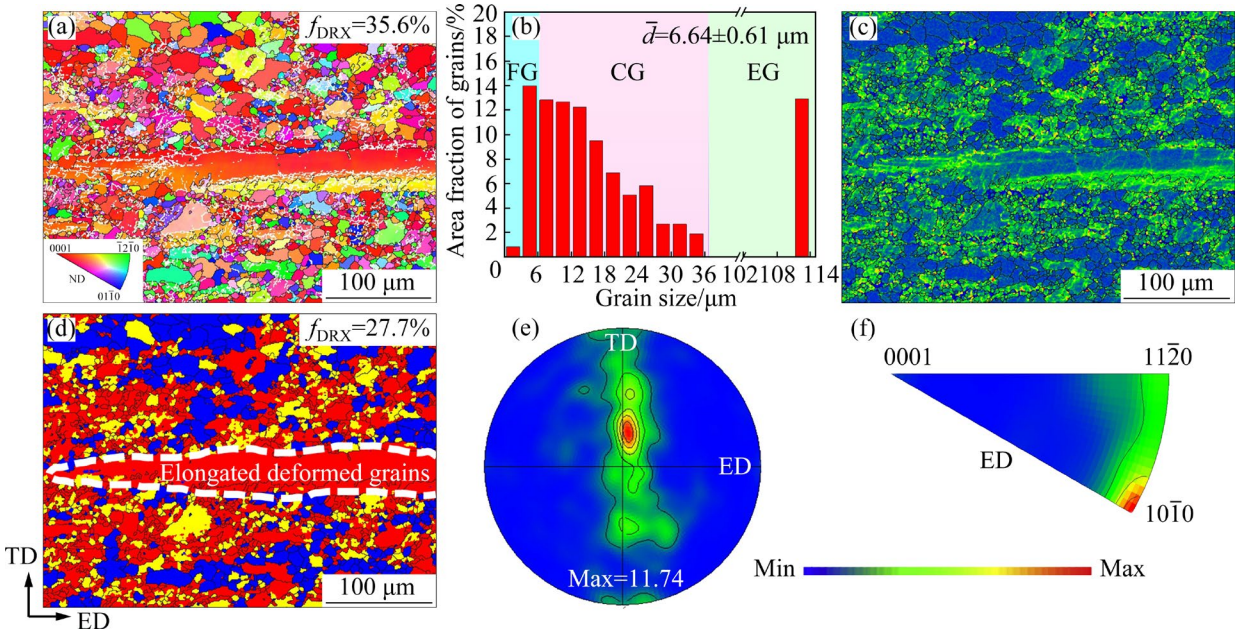

Fig. 3 Grain orientation distribution map (a), grain size distribution map (b), kernel average misorientation (KAM) map (c), deformed structures distribution map (blue: DRXed grains; yellow: Substructured; red: deformed grains) (d), (0001) pole figure (e), and inverse pole figure (f) of extruded Mg−1Bi−0.5Sn−0.5In alloy (TD and ND in the figure represent transverse direction and normal direction, respectively)

coarse equiaxed grains (CGs) of 6−36 μm. A small number of elongated deformed grains (EGs) with sizes larger than 100 μm are also presented along the ED. Figures 3(a, d) reveal that incomplete dynamic recrystallizations (DRX) occur in the sample, owing to the lower extrusion temperature and the presence of numerous nanoscale Mg_3Bi_2 precipitates that delay the DRX process [11]. Moreover, numerous FGs and CGs exhibit large residual strains (Figs. 3(c, d)), which indicates that these grains act as soft zones for further deformation during the extrusion process [22]. Thus, a heterogeneous microstructure consisting of DRXed and deformed grains (EGs and re-deformed DRXed grains) is obtained in the investigated alloy. According to the (0001) pole figure and inverse pole figure along ED in Figs. 3(e, f), respectively, the sample exhibits a strong $(0001)\langle 10\bar{1}0\rangle$ texture, accompanied by a weak basal fiber texture of $\langle 10\bar{1}0\rangle$ //ED.

3.2 DRX behavior

The DRX process is greatly depended on the precursor hardening behavior during the extrusion process. In other words, the initial work hardening and the subsequent strain hardening induced by hetero-deformation require different softening mechanisms, namely DRX mode, to consume the local storage energy and/or coordinate the hetero-deformation. The EGs and their neighboring FGs were selected to further reveal DRX behavior. It can be observed from Fig. 4(a) that several LAGBs and separate HAGBs are presented inside the EGs, which are considered to be evidence of continuous DRX (CDRX) [23,24]. Meanwhile, the dislocation angles from Points *A* to *B* or from Points *C* to *D* are increased by more than 10°, indicating the presence of strong distortion and dislocation accumulations within the grain, which is favorable for the occurrence of CDRX. Moreover, several jagged and bulged grain boundaries are observed around the EGs. In general, the jagged and bulged grain boundaries feature larger local orientations or strain gradients that can function as potential nucleation sites [24]. Such grain boundaries migrate and finally form discontinuous DRX (DDRX) grains. Therefore, several DRXed grains with low storage energy are detected in the vicinity of the EGs, as seen in Fig. 4(e).

The microstructure is separated based on the extent of the grain deformation to further clarify the heterogeneous grain structure. The residual dislocations differ significantly between the DRXed and deformed grains. The geometrically necessary dislocation (GND) density is positively correlated with the KAM value and could be used to characterize the residual dislocation density in these two regions. The GND density is determined by [25]

$$\rho^{\mathrm{GND}}=\frac{2\mathrm{KAM}}{\mu b} \tag{4}$$

where b is the magnitude of Burgers vector (0.32 nm) for Mg alloy and μ is the EBSD step size

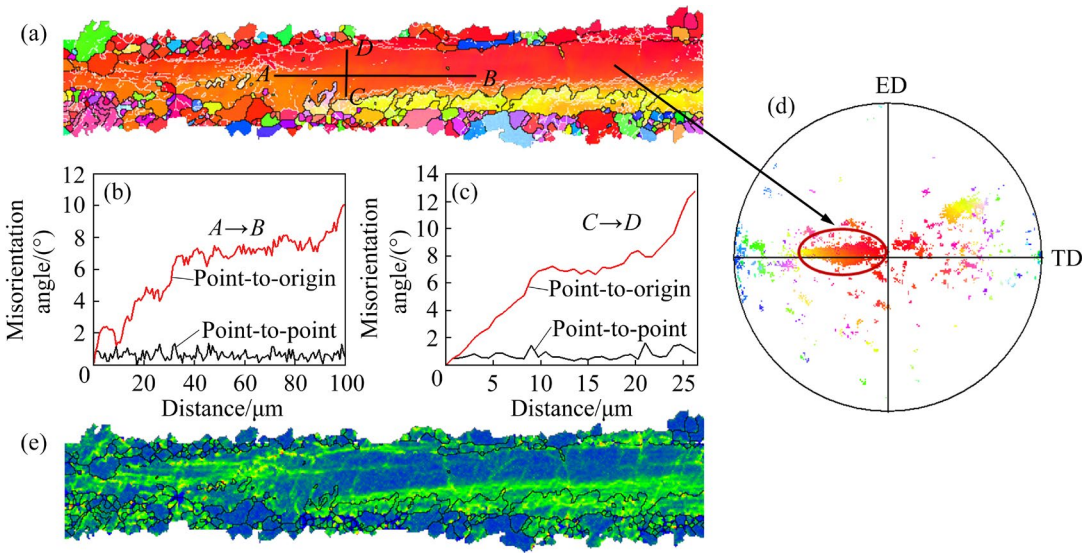

Fig. 4 DRX maps in profiles: (a) EBSD orientation maps; (b, c) Line profiles of misorientation angle; (d) Pole figure; (e) KAM map

(0.75 μm). The column charts of the calculated GND density for different regions are depicted in Figs. 5(b, e). The calculated results indicate that the density of the residual dislocations in the deformed grain regions is about twice as high as that in the DRXed grain regions.

Furthermore, intra-grain misorientation axis (IGMA) analysis is performed for both regions, as illustrated in Figs. 5(c, f). Generally, the activation of basal $\langle a \rangle$ slip and pyramidal $\langle c+a \rangle$ slip leads to IGMA distribution along $\langle 10\bar{1}0 \rangle$ and $\langle 11\bar{2}0 \rangle$, while the activation of prismatic slip leads to IGMA distribution along $\langle 0001 \rangle$ preferentially. The IGMA in the deformed regions is mainly distributed along $\langle 10\bar{1}0 \rangle$ and $\langle 11\bar{2}0 \rangle$, which suggests that the dislocations (0.5°−2°) and LAGBs (2°−15°) are mainly composed of basal $\langle a \rangle$ and/or pyramidal $\langle c+a \rangle$ dislocations [26]. The activation of massive basal slips causes the lattice to rotate about $\langle 10\bar{1}0 \rangle$ Taylor axis, thereby gradually parallelizing the (0001) grain plane to the ED and leading to texture hardening. In comparison, the IGMA distribution in the DRXed grain regions is more random.

3.3 Mechanical properties

Figure 6(a) presents the tensile properties of various Mg alloys. The tensile yield strength (TYS), ultimate tensile strength (UTS) and elongation (EL) are (254.8±3.7) MPa, (315.4±4.9) MPa, and (25.3±1.9)% for extruded alloy and (33.6±2.5) MPa, (109.5±4.2) MPa and (11.8±1.3)% for the as-cast one, respectively. As illustrated in Fig. 6(b), the extruded lean Mg−1Bi−0.5Sn−0.5In alloy exhibits a superior combination of TYS and EL compared to most reported Mg−Al, Mg−Bi, and Mg−RE alloys [10,27−33].

The strain hardening curve indicates that the plastic deformation can be divided into two stages. During the elastic−plastic transformation stage, the strain hardening rate reduces sharply, corresponding to the first stage of strain hardening. Subsequently, the rate decreases slowly with increasing strain, which is the third stage of strain hardening. It can be observed from Table 1 that the average Schmid factor (SF) of the non-basal slip is obviously larger than that of the basal slip, which suggests that the predominant deformation mode is the prismatic $\langle a \rangle$ slip as opposed to the basal $\langle a \rangle$ slip [34]. This contributes to the fact that the strain hardening changes directly from Stage I to Stage III. The EBSD results from the fractured specimen show that the peak of IGMA with an orientation difference of 0.5°−2° occurs near (0001), indicating the activation of a large amount of prismatic $\langle a \rangle$ slip, which further supports the above conclusion. In addition, a small amount of IGMA is distributed along $\langle 10\bar{1}0 \rangle$ and $\langle 11\bar{2}0 \rangle$, demonstrating that basal $\langle a \rangle$ and/or pyramidal $\langle c+a \rangle$ slips are also activated at the later deformation stage, but the contribution is relatively small.

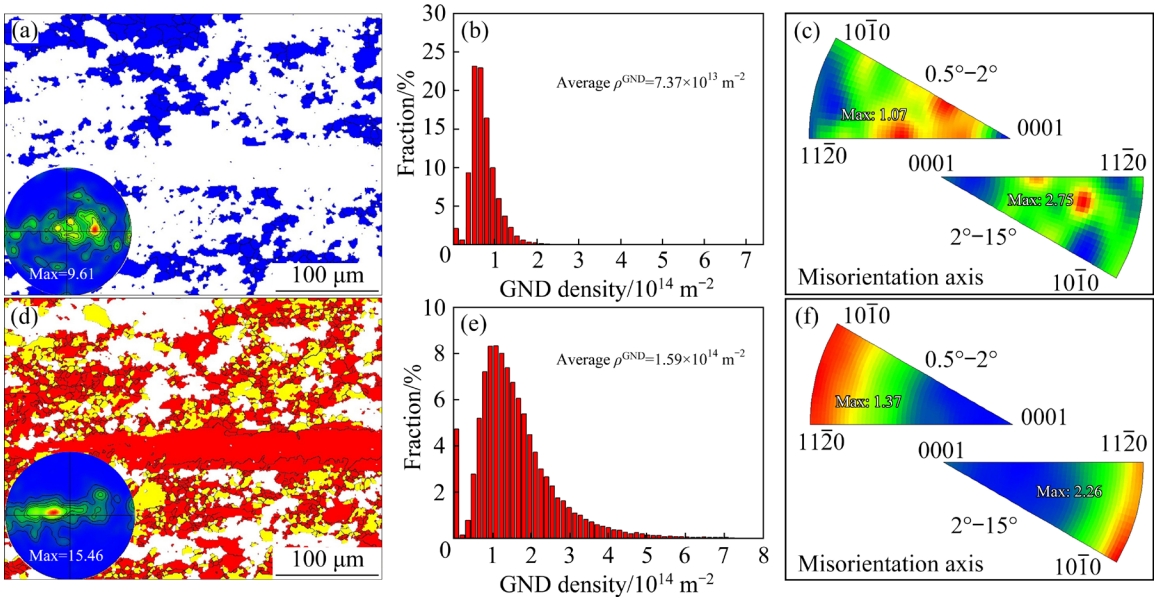

Fig. 5 DRXed grain (a) and deformed grain (d) distributions with (0001) pole figure of extruded alloy and corresponding GND density distributions (b, e); IGMA results for DRXed (c) and deformed (f) regions

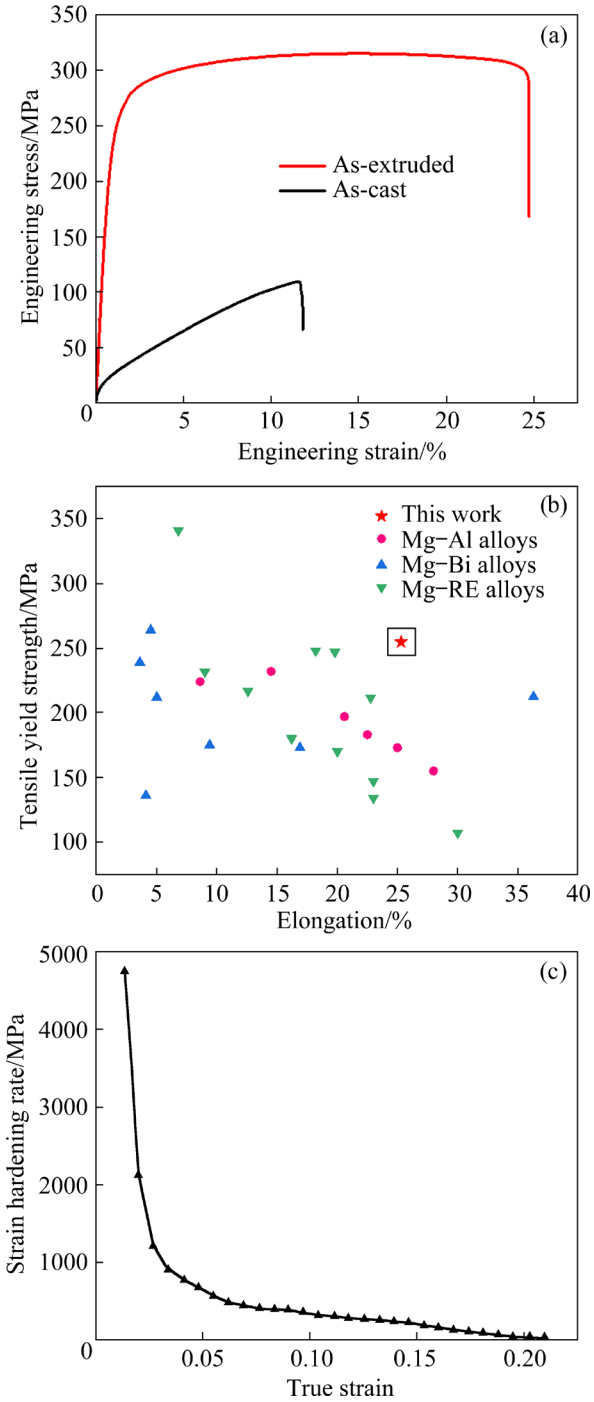

Fig. 6 Engineering tensile stress−strain curve (a), comparison of TYS vs EL of various Mg alloys (b) and strain hardening rate curve of tensile sample (c)

Table 1 Average SF values for various slip systems with different grain structures

Grain structure	Basal ⟨*a*⟩	Prismatic ⟨*a*⟩	Pyramidal ⟨*c*+*a*⟩
FG	0.196	0.429	0.401
CG	0.191	0.433	0.404
EG	0.099	0.435	0.381

Figure 7(c) depicts the SEM morphology of the fracture surface. The morphology is dominated by ductile fracture, which is associated with numerous small and shallow dimples. Several fine precipitates can be observed in these dimples. Moreover, the presence of a small number of brittle fracture zones can be related to the cracking of CGs.

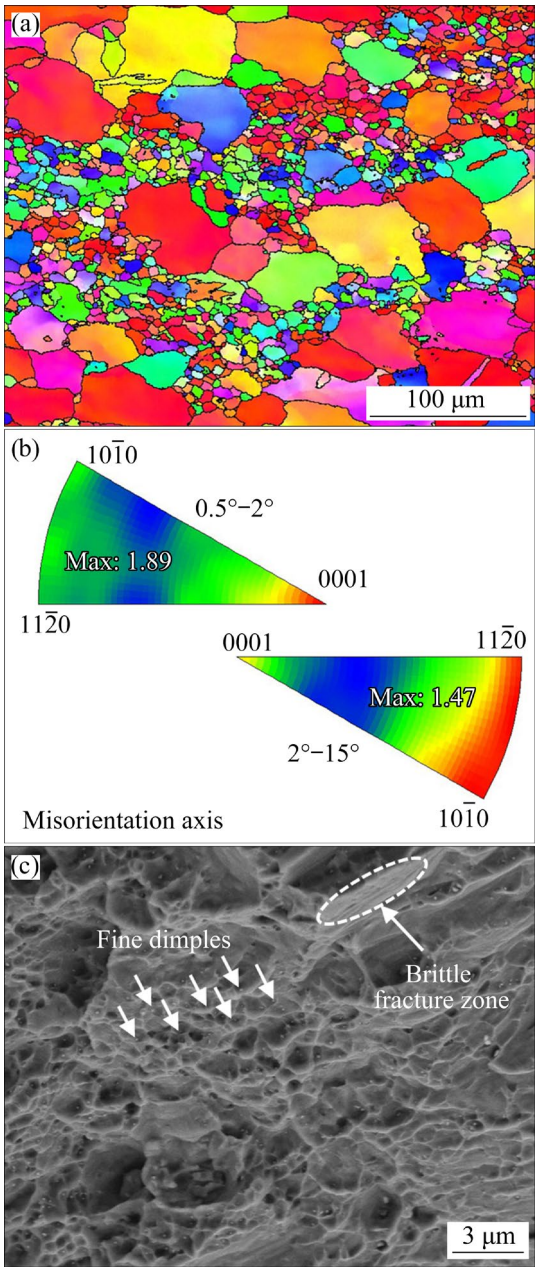

Fig. 7 IPF map of fractured specimen (a), IGMA map (b) and SEM image of fracture surfaces (c) of tensile sample

3.4 Electrochemical behavior

The polarization curves of the investigated alloy after immersion are presented in Fig. 8(a) to estimate the transient polarization response. Owing

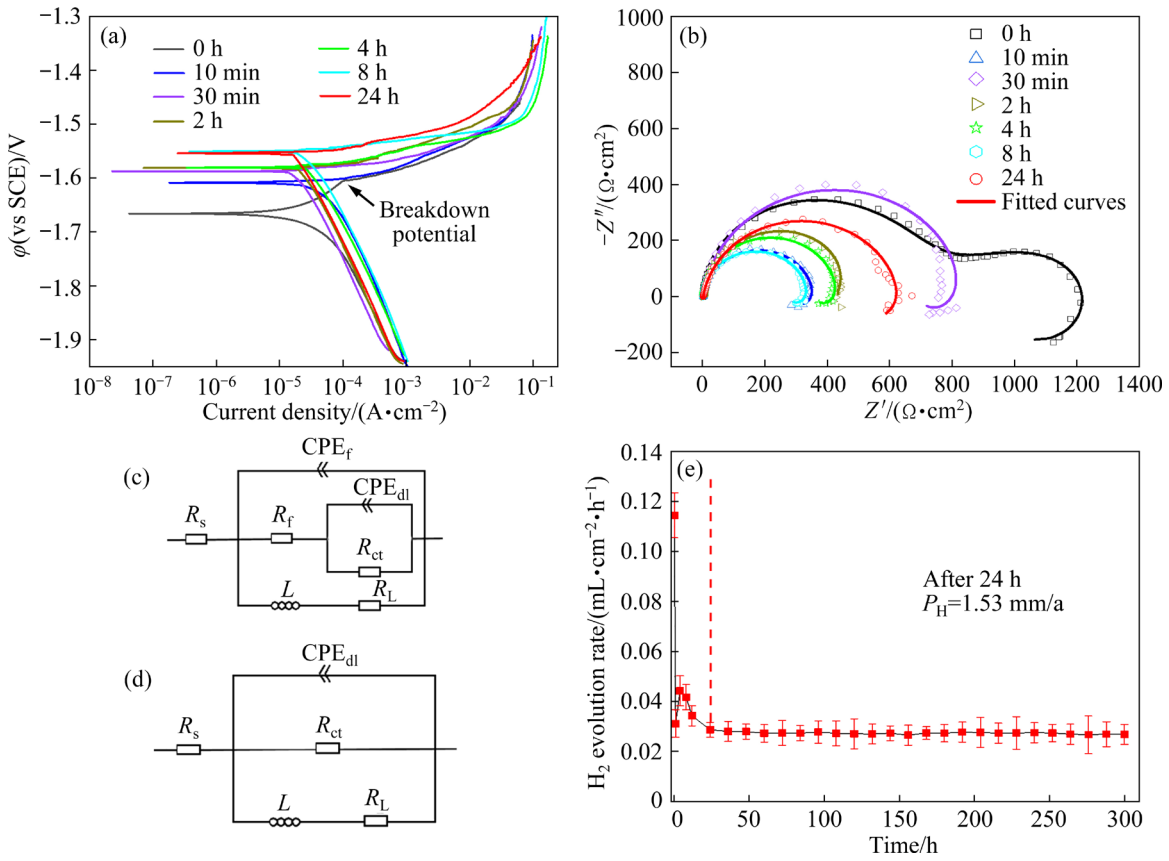

Fig. 8 Polarization curves (a), Nyquist spectra following immersion for 0 h, 10 min, 30 min, 2 h, 4 h, 8 h, and 24 h (b), equivalent circuit diagrams (c, d), and average hydrogen evolution rate for different durations (e)

to the passivation of the Mg alloy in the anodic dissolution process, the anodic polarization branch is curved. Therefore, the cathodic Tafel extrapolation method [35] is adopted to evaluate the corrosion current density (J_{corr}), and the results are exhibited in Table 2. With increasing immersion time, φ_{corr} shifts in a positive direction, with values varying from −1.666 V in the initial stage to −1.554 V after 24 h. The current density during the immersion process exhibits an overall decreasing trend, achieving 20.8 μA/cm^2 (P_i=0.47 mm/a) by 24 h, and the variations in the intermediate process are related to the corrosion product film. Moreover, pseudo-passivation behavior, which features a moderate increase in the current density as the potential shifts, appears on the anodic branches of the unsoaked (0 h) specimen. When the potential exceeds the breakdown potential, the corrosion current density increases rapidly due to the destroyed surface film.

In Fig. 8(b), the Nyquist spectra for the initial 10 min immersion consist of a capacitance, a capacitance and an inductance loop at high, medium as well as low frequency, respectively. Nevertheless, the shape of the Nyquist spectrum changes as the immersion time exceeds 10 min, exhibiting capacitive and inductive loops at high and low frequencies, respectively, due to the formation and dissolution of the surface corrosion product films. The EIS data are fitted by the ZsimpWin software with the equivalent circuit maps in Figs. 8(c, d), summarized in Table 3. In the equivalent circuit, R_s denotes solution resistance, R_f and CPE_f correspond to the surface film resistance

Table 2 Critical fitting results from polarization curves

Period	φ_{corr} (vs SCE)/V	J_{corr}/(μA·cm^{-2})	P_i/(mm·a^{-1})
0 h	−1.666±0.016	48.5±3.6	1.098±0.081
10 min	−1.609±0.012	57.7±2.9	1.306±0.066
30 min	−1.588±0.021	22.3±2.3	0.505±0.052
2 h	−1.581±0.029	26.8±2.5	0.606±0.057
4 h	−1.581±0.016	35.4±3.1	0.801±0.070
8 h	−1.551±0.015	34.1±3.3	0.772±0.074
24 h	−1.554±0.022	20.8±1.9	0.471±0.043

Table 3 Fitting parameters from EIS data recorded after various immersion time of studied alloy

Period	R_s/ ($\Omega\cdot cm^2$)	CPE_{dl}		R_{ct}/ ($\Omega\cdot cm^2$)	CPE_f		R_f/ ($\Omega\cdot cm^2$)	L/ ($H\cdot cm^2$)	R_L/ ($\Omega\cdot cm^2$)	χ^2/ 10^{-3}
		Q/($\mu F\cdot S^{(p-1)}\cdot cm^{-2}$)	n_{dl}		Q/($\mu F\cdot S^{(p-1)}\cdot cm^{-2}$)	n_f				
0 h	1.64	11.2	0.84	339.8	10.6	0.98	523.0	11720	551.9	3.56
10 min	2.97	15.7	0.95	356.1	−	−	−	258.3	1405	2.53
30 min	3.09	16.2	0.93	846.7	−	−	−	873.6	3931	2.31
2 h	2.80	20.4	0.94	525.2	−	−	−	55.64	2437	5.26
4 h	1.75	25.3	0.98	434.1	−	−	−	589.8	2124	5.27
8 h	2.15	31.1	0.97	336.9	−	−	−	520.2	1562	8.38
24 h	2.37	23.1	0.90	631.6	−	−	−	1842	1681	5.18

and capacitor, respectively, and R_{ct} and CPE_{dl} represent the charge transfer resistance and electric double-layer capacitance, respectively, at high frequency [23].

In the low-frequency regions, L and R_L are the inductance and inductive resistance, respectively, with reference to the rupture of the partially corroded product film and the onset of localized pitting corrosion [36]. The evolution of R_{ct} during the immersion test can be characterized by three stages. In Stage I (0−30 min), R_{ct} increases gradually owing to the generation of the oxide film. In Stage II (0.5−8 h), R_{ct} decreases rapidly to a smaller value owing to the onset of localized corrosion. However, R_{ct} increases again in Stage III (8−24 h), which means a possible occurrence of the re-passivation process [5] and the formation of a corrosion-resistant surface film. To further determine the corrosion rate of the alloys, hydrogen evolution tests are performed and presented in Fig. 8(e). As it can be seen, the hydrogen evolution rate tends to stabilize after 24 h of immersion, from which the corrosion rate (P_H) is calculated as 1.53 mm/a.

4 Discussion

4.1 Strengthening−plasticity mechanisms

The extruded alloy shows superior strength−ductility synergy, which is mainly related to the grain structure, texture, precipitated particles, and dislocations. As the microstructures (such as texture, dislocations, and twins) of the recrystallized and deformed regions in this study differ significantly, the effects on the mechanical properties are discussed in detail from the perspective of the recrystallized and deformed regions.

The yield strength (σ_y) for the extruded Mg−1Bi−0.5Sn−0.5In alloy with a heterogeneous grain structure could be quantitatively described as [9,20,37,38].

$$\sigma_y=\sigma_{cast}+\Delta\sigma_{GB}+\Delta\sigma_T+f_{DRX}M_{DRX}(\Delta\tau_P+\Delta\tau_{\rho,DRX})+ f_dM_d(\Delta\tau_P+\Delta\tau_{\rho,d}) \quad (5)$$

where σ_{cast} represents the TYS of the as-cast Mg−1Bi−0.5Sn−0.5In alloy (33.6 MPa; Fig. 6(a)); $\Delta\sigma_{GB}$ is the strength increment via grain boundary strengthening; $\Delta\sigma_T$ is the strength increment via texture strengthening; f_{DRX} and f_d are the area fractions for the DRXed and deformed regions, respectively; M is the Taylor factor, and the values of M_{DRX} and M_d are 2.5 and 4 for the DRXed and deformed regions with large disparities in texture intensity, respectively [9]; $\Delta\tau_P$ and $\Delta\tau_\rho$ are the critical resolved shear stress (CRSS) contributions resulting from the precipitation and dislocation strengthening, respectively. The solid solution strengthening is omitted because it contributes little to the TYS owing to the lower extent of alloying.

The grain boundary strengthening effect from the EGs is weak and can be ignored. Therefore, the contribution of the grain refinement strengthening to the TYS could be calculated as follows:

$$\Delta\sigma_{GB}=(1-f_e)kd^{-1/2} \quad (6)$$

where f_e is the area fraction (12.9%) of the elongated deformed regions, k is the Hall−Petch coefficient, and d is the average grain size (6.64 μm) of equiaxial grain regions. According to the previous study [39], the value of k is assumed to be approximately 290 $MPa\cdot\mu m^{1/2}$. Hence, the estimated increment in the TYS resulting from the grain boundaries is 98.0 MPa.

Given the significant disparities in texture between the DRXed and the deformed grains

(Fig. 5), the effect of texture on the TYS could be characterized by [20]

$$\Delta\sigma_T=f_{DRX}m_{DRX}\tau_0+f_dm_d\tau_0 \quad (7)$$

where m_{DRX} (=62.5) and m_d (=100.5) are the orientation factors related to the basal texture, which are 6.5 times of the basal texture intensity for the DRXed and deformed grains, respectively, and τ_0 is the CRSS of the activated slip systems. Based on previous studies [40], the value of τ_0 lies between 0.6 and 4.0 MPa, and a minimal value is adopted owing to the lower extent of alloying in this work. Consequently, the calculated $\Delta\sigma_T$ is approximately 54.2 MPa.

In this study, numerous fine Mg_3Bi_2 particles are presented in the alloy, and the improvement in the CRSS ($\Delta\tau_P$) for the basal slip contributed by the precipitation strengthening could be expressed as follows [20]:

$$\Delta\tau_P=\frac{0.4Gb}{\pi\sqrt{1-\upsilon}}\frac{\ln\left(2\overline{r}/b\right)}{\lambda_P} \quad (8)$$

where G is the shear modulus (16.6 GPa), b is the magnitude of Burgers vector (0.32 nm), υ is the Poisson's ratio (0.267), $\lambda_P\left(=2\overline{r}\left(\sqrt{\pi/(4f_P)}-1\right)\right)$ is the inter-precipitate spacing, f_P is the volume fraction (2.59%), $\overline{r}=\sqrt{3/2}r$, and r is the radius (51 nm) of the precipitates. Furthermore, f_P and r are evaluated by the Image-Pro Plus 6.0 software from three SEM pictures ranging in area from 50 μm × 50 μm, and an average value is obtained. Hence, the value of $\Delta\tau_P$ is approximately 8.3 MPa.

A larger dislocation density appears in the deformed regions than in the DRXed regions, as illustrated in Figs. 5(b, e). The dislocation strengthening exhibits the following general relationship with the dislocation density [37]:

$$\Delta\tau_\rho=\alpha Gb\sqrt{\rho^{GND}} \quad (9)$$

where α is a constant that is assumed to be 0.2 and ρ^{GND} represents the dislocation density. Thus, the values of $\Delta\tau_{\rho,DRX}$ and $\Delta\tau_{\rho,d}$ are approximately 9.1 and 13.4 MPa, respectively.

The contributions of the above-mentioned strengthening mechanisms are exhibited in Table 4. A comparison of the calculated TYS and the experimental values reveals that they are almost equal within the error range. It appears that the grain boundary strengthening induced by the equiaxial grains is responsible for the largest part (37.8%) of the overall strengthening in the Mg−1Bi−0.5Sn−0.5In alloy. Texture, precipitation, and dislocation strengthening also play essential roles in the strength of the alloy.

Furthermore, the ductility of the alloy is excellent. This phenomenon is generally associated with the activation of multi-slip systems [26,34]. The activation of the slip system is mainly influenced by the precipitates, texture, and grain size distribution when Mg alloy deformation occurs at room temperature [34]. In this work, the effects of the dynamic precipitates on ductility are limited owing to their small size and low density. As this alloy has a strong basal texture, the activation of the basal slip is difficult during tension along the ED. Under such circumstances, prismatic slip, as additional deformation mode, can be activated and involved in the plastic deformation with increasing stress. Furthermore, the synergistic effect of the bimodal grain structure during the deformation process guarantees favorable strain coordination capability. These factors contribute to the superior strength−ductility synergy of this alloy.

4.2 Corrosion mechanisms

SEM characterizations are performed on the specimens exposed to the 3.5 wt.% NaCl solution for various time to clarify the corrosion mechanism of the investigated alloy. The partial enlargement of Fig. 9(a) shows that after 5 min of immersion, local corrosion happens in the α-Mg matrix around the Mg_3Bi_2 particles, owing to the higher corrosion potential of the Mg_3Bi_2 particles compared to that of the α-Mg matrix. The corrosion spreads further after immersion for 30 min and a film of corrosion products can be observed. After 1 h of immersion, the product film is gradually eroded owing to its

Table 4 Calculated values from different strengthening mechanisms of Mg−1Bi−0.5Sn−0.5In alloy (MPa)

σ_{cast}	$\Delta\sigma_{GB}$	$\Delta\sigma_T$		$\Delta\sigma_P$		$\Delta\sigma_\rho$		$\Delta\sigma_{sum}$
		$\Delta\sigma_{T,DRX}$	$\Delta\sigma_{T,d}$	$\Delta\sigma_{P,DRX}$	$\Delta\sigma_{P,d}$	$\Delta\sigma_{\rho,DRX}$	$\Delta\sigma_{\rho,d}$	
33.6	98.0	10.4	43.8	4.7	24.0	6.3	38.7	259.5

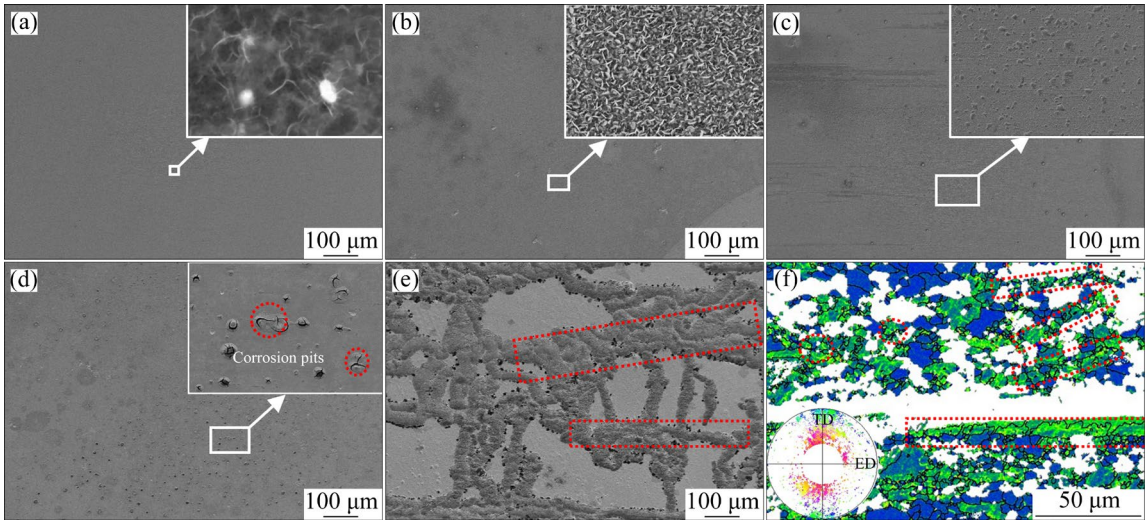

Fig. 9 SEM micrographs of extruded alloy immersed for 5 min (a), 30 min (b), 1 h (c), 2 h (d), 4 h (e), along with KAM map of non-basal oriented grains (f)

weak protective effect. After immersion for 2 h, numerous corrosion pits are observed. According to previous studies [41], the (0001) basal plane exhibits better corrosion resistance than the non-basal plane, which is attributed to the high atomic coordination with the high binding energy of the former. Accordingly, the density functional theory (DFT) results (Table 5) confirm that the stripping of the Mg atoms on Mg (0001) requires higher energy (0.8634 eV) than that on the $(10\bar{1}2)$ (0.3272 eV) and $(1\bar{1}00)$ (0.0398 eV) planes, suggesting that the Mg atoms on the $(10\bar{1}2)$ and $(1\bar{1}00)$ planes are stripped preferentially than those on the (0001) basal plane during the corrosion process.

Table 5 Mg atom stripping energy from different crystal planes (eV)

(0001)	$(1\bar{1}00)$	$(10\bar{1}2)$
0.8634	0.3272	0.0398

In this study, grains with the (0001) crystal plane deflected by 30°−90° are defined from the ND as non-basal plane grains (Fig. 9(f)), which are more susceptible to corrosion than the basal plane grains. Furthermore, corrosion is more likely to occur at the grain boundaries and dislocations where higher energy and severe lattice distortion are present [8]. Therefore, it can be reasonably inferred that the micro-galvanic corrosion can intensify between the non-basal FG region with high-density dislocation and neighboring region, thus forming serious pitting corrosion, such as some of the FGs marked by circles in Fig. 9(f). After an immersion time of 4 h, the corrosion propagates preferentially along the FG regions of the high-density dislocation marked in the rectangle in Fig. 9(f), and the corrosion morphology is mainly manifested as filiform corrosion (Fig. 9(e)).

The standard potentials of Mg, Bi, Sn, and In are −2.37, +0.31, −0.14, and −0.34 V, respectively. Therefore, the dissolution of the Bi, Sn, and In in the α-Mg matrix can reduce the electrochemical corrosion tendency of the matrix. Moreover, the presence of Mg_3Bi_2 with Volta potential of approximately 120−150 mV higher than that of the Mg matrix [8,42], and thus numerous micro-galvanic couples can be generated between the Mg_3Bi_2 particles and α-Mg matrix during immersion, leading to the preferential dissolution of the matrix around Mg_3Bi_2, as illustrated in Fig. 9(a). Therefore, the contact region between the Mg_3Bi_2 particles and electrolyte increases and the Mg_3Bi_2 particles are corroded subsequently after the dissolution of the α-Mg matrix.

The kinetic parameters, especially of the passive film, which can notably affect the corrosion rate, should also be considered in the corrosion process. The morphology and composition of the corrosion product in the specimens immersed for 4 and 24 h are characterized by SEM and XPS. The corrosion products cover the sample surface uniformly after 24 h of immersion (Fig. 10(c)) with the propagation of filiform corrosion. Figure 11(a) indicates that the Mg 1s spectrum consists of three

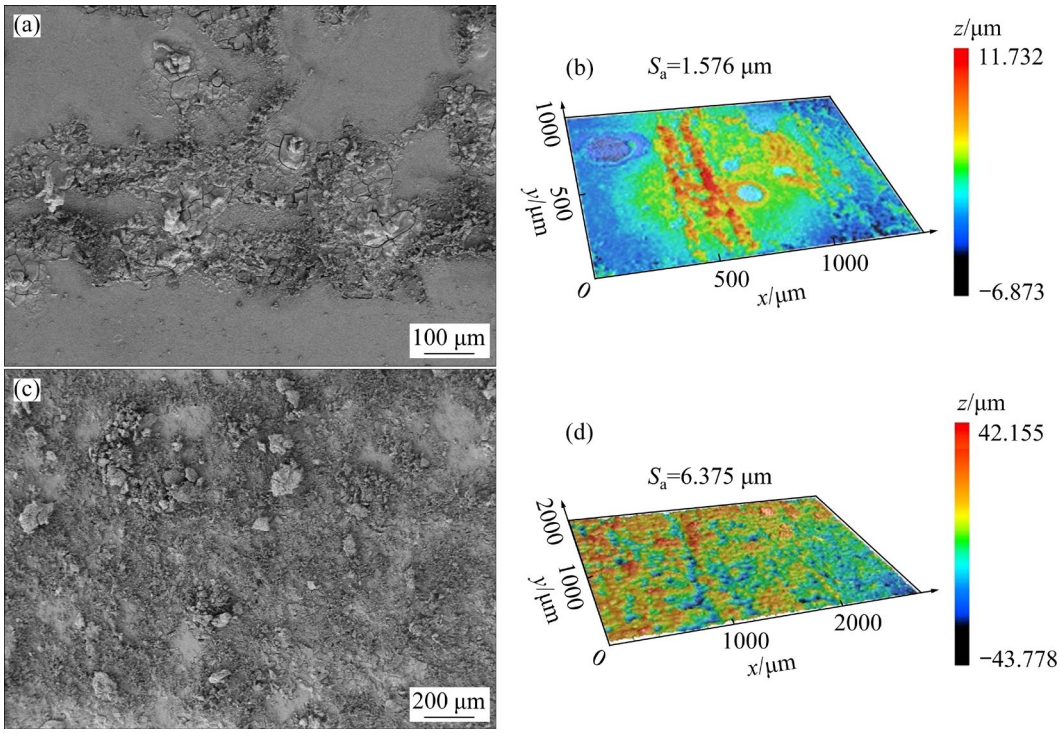

Fig. 10 SEM micrographs with corrosion products (a, c) and 3D tomographic maps without corrosion products (b, d) on studied alloy after immersion in NaCl solution for 4 h (a, b) and 24 h (c, d)

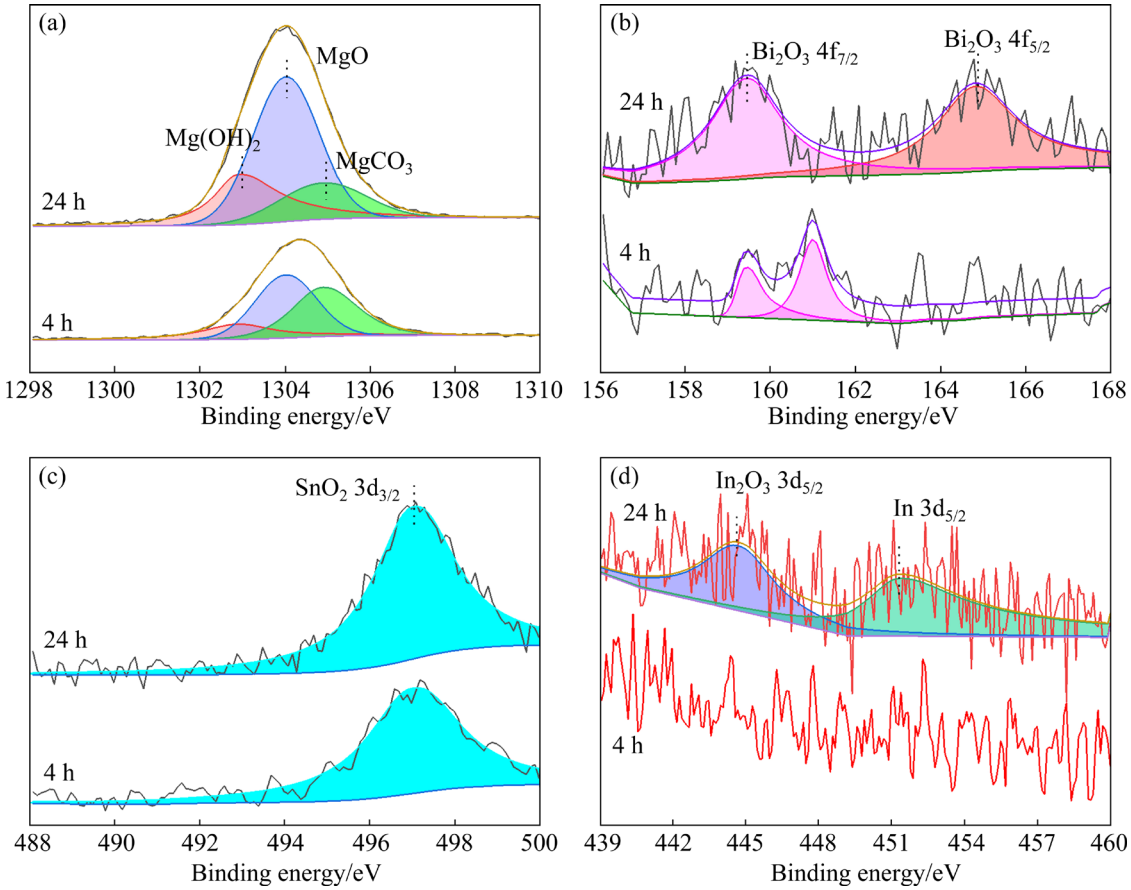

Fig. 11 XPS spectra of surface oxide films after immersion in NaCl solution for 4 h and 24 h: (a) Mg 1s; (b) Bi 4f; (c) Sn 3d; (d) In 3d

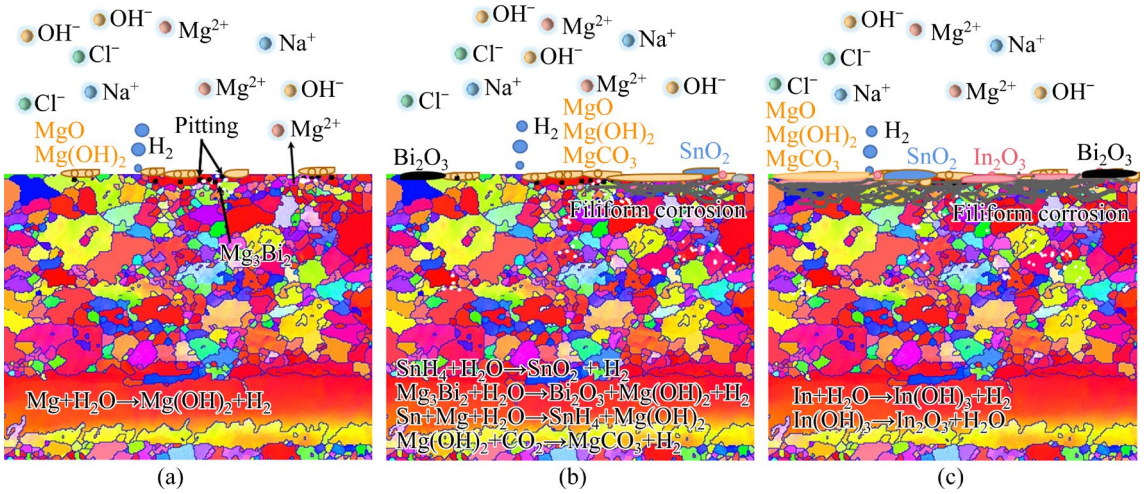

Fig. 12 Corrosion mechanisms of studied alloys in NaCl solution: (a) Initial immersion period; (b) After 4 h; (c) After 24 h

peaks, which are regarded as $Mg(OH)_2$, MgO, and $MgCO_3$. The formation of $MgCO_3$ is ascribed to the dissolution of CO_2 from air in the NaCl solution [43]. The protective properties of the oxide films are associated with the Pilling−Bedworth ratio (PBR) primarily [44]. Some level of compressive stress arises on the surface oxide film for PBR values between 1 and 2, and such films are relatively compact. Tensile stress or excess compressive stress is generated on the oxide film for PBR values less than 1 or more than 2, which is prone to film rupture. Owing to the PBR values of 0.80 and 2.04 for the MgO and $MgCO_3$, respectively, and the fact that the $Mg(OH)_2$ is loose and porous, the passive films that are formed during the early stage of immersion provide poor protection to the matrix. Although SnO_2 and Bi_2O_3 with stronger protection [45,46] are formed after 4 h of immersion (Figs. 11(b, c)), the content is relatively low and the corrosion rate is not varied obviously. After 24 h of immersion, the contents of the SnO_2 and Bi_2O_3 increase and In_2O_3 [16] is formed (Fig. 11(d)). The resulting composite oxide film can fully block the penetration of the corrosive medium, and thus effectively protects the internal matrix against corrosion, which is the reason for the sufficient occurrence of re-passivation.

Figures 10(b, d) show the 3D corrosion morphologies after different immersion periods in 3.5 wt.% NaCl solution without corrosion products. After an immersion time of 4 h, the typical filament features can be observed on the specimen surface, as the evidence of filiform corrosion. After immersion for 24 h, the surface of the specimen is already covered with filiform corrosion. The corrosion mechanism of the specimen is illustrated in Fig. 12. In the initial immersion period, corrosion occurs preferentially in the matrix around the Mg_3Bi_2 particles and gradually develops into pitting corrosion. Due to the low stripping energy of non-basal grains and the high energy of grain boundaries and dislocation regions, the pitting corrosion propagates along the area of fine non-basal grains with high density dislocations and develops into filiform corrosion, during which composite oxide films (SnO_2−Bi_2O_3−In_2O_3) are formed, which can retard the corrosion process effectively.

5 Conclusions

(1) The extruded lean Mg−1Bi−0.5Sn−0.5In alloy exhibits a heterogeneous microstructure consisting of DRXed and deformed grains (EGs and re-deformed DRXed grains).

(2) The extruded lean Mg−1Bi−0.5Sn−0.5In alloy exhibits high strength−ductility synergy (TYS of 254.8 MPa, UTS of 315.4 MPa, and EL of 25.3%) and corrosion resistance (P_i=0.47 mm/a and P_H= 1.53 mm/a).

(3) The grain boundary strengthening caused by equiaxed grains contributes the most to the overall strengthening. The favorable ductility is mainly associated with the activation of prismatic slip, and enhancement of strain coordination capability.

(4) The micro-galvanic corrosion is intensified between the FG region with high-density dislocation and the neighboring region, thus forming serious pitting corrosion at the initial stage, and propagates along these regions to develop filiform corrosion. Protective composite oxide film (SnO_2−Bi_2O_3−In_2O_3) is formed after 24 h of immersion, which delays the corrosion process.

CRediT authorship contribution statement

Hong-wei XU: Conceptualization, Investigation, Formal analysis, Writing − Original draft, Writing − Review & editing; **Wen-ting XU:** Validation, Formal analysis, Writing − Review & editing; **Wei-li CHENG:** Conceptualization, Supervision, Project administration, Writing – Review & editing; **Jian LI:** Funding acquisition, Resources; **Li-fei WANG:** Methodology, Writing – Review & editing; **Hui YU:** Formal analysis, Writing − Review & editing; **Jin-hui WANG:** Supervision; **Hua HOU:** Supervision; **Kwang Seon SHIN:** Supervision.

Declaration of competing interest

The authors declare that they have no known competing financial interests or personal relationships that could have appeared to influence the work reported in this paper.

Acknowledgments

This study was partially supported by the National Natural Science Foundation of China (No. 51901153), the Natural Science Foundation of Shanxi, China (No. 202103021224049), the Shanxi Zhejiang University New Materials and Chemical Research Institute Scientific Research Project, China (No. 2022SX-TD025), and the Open Project of Salt Lake Chemical Engineering Research Complex, Qinghai University, China (No. 2023-DXSSKF-Z02).

References

[1] LI Z H, GAO S, SASAKI T T, NAKATA T, KAMADO S, TSUJI N, HONO K. Discontinuous yielding phenomena triggered by Zn addition in low-alloyed Mg−Al−Ca−Mn alloys [J]. Scripta Materialia, 2022, 211: 114967.

[2] PAN Hu-cheng, KANG Rui, LI Jing-ren, XIE Hong-bo, ZENG Zhuo-ran, HUANG Qiu-yan, YANG Chang-lin, REN Yu-ping, QIN Gao-wu. Mechanistic investigation of a low-alloy Mg−Ca-based extrusion alloy with high strength−ductility synergy [J]. Acta Materialia, 2020, 186: 278−290.

[3] DULEY P, BAIRAGI D, BAIRI L R, BANDYOPADHYAY T K, MANDAL S. Effect of microstructural evolution and texture change on the in-vitro bio-corrosion behaviour of hard-plate hot forged Mg−4Zn−0.5Ca−0.16Mn (wt.%) alloy [J]. Corrosion Science, 2021, 192: 109860.

[4] SUN Yue-hua, WANG Ri-chu, PENG Chao-qun, WANG Xiao-feng. Effect of Gd on microstructure, mechanical properties, and corrosion behavior of as-homogenized Mg−8Li−3Al−2Zn−0.2Zr alloy [J]. Transactions of Nonferrous Metals Society of China, 2022, 32: 2494−2509.

[5] ZHENG Qiu-ju, WU Jing, JIANG Hong-xiang, ZHANG Li-li, ZHAO Jiu-zhou, HE Jie. Effect of micro-alloying element La on corrosion behavior of Al−Mg−Si alloys [J]. Corrosion Science, 2021, 179: 109113.

[6] YU Hui, FAN Shao-da, MENG Shuai-ju, CHOI J O, LI Zhong-jie, GO Y, KIM Y M, ZHAO Wei-min, YOU B S, SHIN K S. Microstructural evolution and mechanical properties of binary Mg−*x*Bi (*x*=2, 5, and 8 wt.%) alloys [J]. Journal of Magnesium and Alloys, 2021, 9: 983−994.

[7] LI Feng, CHENG Wei-li, YU Hui, WANG Hong-xia, NIU Xiao-feng, WANG Li-fei, LI Hang, HOU Hua. Corrosion behavior and mechanical properties of extruded low-alloyed Mg−0.5Bi−0.5Y−0.2Zn alloy [J]. Transactions of Nonferrous Metals Society of China, 2023, 33: 743−754.

[8] LIU Yang, CHENG Wei-li, GU Xiong-jie, LIU Yan-hui, CUI Ze-qin, WANG Li-fei, WANG Hong-xia. Tailoring the microstructural characteristic and improving the corrosion resistance of extruded dilute Mg−0.5Bi−0.5Sn alloy by microalloying with Mn [J]. Journal of Magnesium and Alloys, 2021, 9: 1656−1668.

[9] LUO Yi-hao, CHENG Wei-li, LI Hang, YU Hui, WANG Hong-xia, NIU Xiao-feng, WANG Li-fei, YOU Zhi-yong, HOU Hua. Achieving high strength-ductility synergy in a novel Mg−Bi−Sn−Mn alloy with bimodal microstructure by hot extrusion [J]. Materials Science and Engineering A, 2022, 834: 142623.

[10] JIN S C, CHA J W, LEE J H, LEE T, HAN S H, PARK S H. Improvement in tensile strength of extruded Mg−5Bi alloy through addition of Sn and its underlying strengthening mechanisms [J]. Journal of Magnesium and Alloys, 2021, 10: 3100−3112.

[11] JIN S C, LEE J U, GO J, YU H, PARK S H. Effects of Sn addition on the microstructure and mechanical properties of extruded Mg−Bi binary alloy [J]. Journal of Magnesium and Alloys, 2022, 10: 850−861.

[12] ESMAILY M., SVENSSON J E, FAJARDO S, BIRBILIS N, FRANKEL G S, VIRTANEN S, ARRABAL R, THOMAS S, JOHANSSON L G. Fundamentals and advances in magnesium alloy corrosion [J]. Progress in Materials Science, 2017, 89: 92−193.

[13] KUBASEK J, VOJTECH D, LIPOV J, RUML T. Structure, mechanical properties, corrosion behavior and cytotoxicity of biodegradable Mg−X (X=Sn, Ga, In) alloys [J]. Materials Science and Engineering C, 2013, 33: 2421−2432.

[14] SONG Guang-ling. Effect of tin modification on corrosion of AM70 magnesium alloy [J]. Corrosion Science, 2009, 51: 2063−2070.

[15] CHEN Ji-hua, CHEN Zhen-hua, YAN Hong-ge, ZHANG Fu-quan, LIAO Kun. Effects of Sn addition on microstructure and mechanical properties of Mg−Zn−Al alloys [J]. Journal of Alloys and Compounds, 2008, 461:

209−215.

[16] WANG Xue-jian, CHEN Zong-ning, REN Jing, KANG Hui-jun, GUO En-yu, LI Jie-hua, WANG Tong-min. Corrosion behavior of as-cast Mg−5Sn based alloys with In additions in 3.5 wt.% NaCl solution [J]. Corrosion Science, 2020, 164: 108318.

[17] YIN Ming, HOU Li-feng, WANG Zhi-wei, BAO Tong-yao, LIU Bao-sheng, WEI Huan, LIU Xiao-da, DU Hua-yun, WEI Ying-hui. Self-generating construction of applicable corrosion-resistant surface structure of magnesium alloy [J]. Corrosion Science, 2021, 184: 109378.

[18] ZHANG De-ping, ZHANG Dong-dong, XU Tao, CHEN Shan-rong, ZHANG Ya-qin, LI Xin-lin, ZHANG Jin-hui. Achieving high-strength in Mg−0.8Zn−0.2Zr (wt.%) alloy extruded at low temperature [J]. Materials Science and Engineering A, 2021, 822: 141657.

[19] WU Xiao-lei, YANG Mu-xin, YUAN Fu-ping, WU Gui-lin, WEI Yu-jie, HUANG Xiao-xu, ZHU Yun-tian. Heterogeneous lamella structure unites ultrafine-grain strength with coarse-grain ductility [J]. Proceedings of the National Academy of Sciences of the United States of America, 2015, 112: 14501−14505.

[20] GUO Zhen-yu, CHENG Wei-li, WANG Hong-xia, YU Hui, NIU Xiao-feng, WANG Li-fei, LI Hang, HOU Hua. Insight on the correlation between bimodal-sized grain structure and tensile properties of extruded low-alloyed Mg−Sn−Bi−Mn alloy [J]. Materials Science and Engineering A, 2022, 843: 143128.

[21] SUN Yue-hua, WANG Ri-chu, PENG Chao-qun, CAI Zhi-yong. Microstructure and corrosion behavior of as-extruded Mg−xLi−3Al−2Zn−0.2Zr alloys (x = 5, 8, 11 wt.%) [J]. Corrosion Science, 2020, 167: 108487.

[22] GUO Fei, ZHANG Ding-fei, WU Hua-yi, JIANG Lu-yao, PAN Fu-sheng. The role of Al content on deformation behavior and related texture evolution during hot rolling of Mg−Al−Zn alloys [J]. Journal of Alloys and Compounds, 2017, 695: 396−403.

[23] TANG Jian-wei, CHEN Liang, LI Zhi-gang, ZHAO Guo-qun, ZHANG Cun-sheng, LIN Jun, ZUO Yang. Microstructure characterization and corrosion behavior of hollow ZK60 Mg profile containing longitudinal welds [J]. Corrosion Science, 2021, 193: 109875.

[24] CHENG Wei-li, BAI Yang, MA Shi-chao, WANG Li-fei, WANG Hong-xia, YU Hui. Hot deformation behavior and workability characteristic of a fine-grained Mg–8Sn–2Zn–2Al alloy with processing map [J]. Journal of Materials Science & Technology, 2019, 35: 1198−1209.

[25] YAN Zhi-feng, WANG Deng-hui, HE Xiu-li, WANG Wen-xian, ZHANG Hong-xia, DONG Peng, LI Chen-hao, LI Yu-li, ZHOU Jun, LIU Zhuang, SUN Li-yong. Deformation behaviors and cyclic strength assessment of AZ31B magnesium alloy based on steady ratcheting effect [J]. Materials Science and Engineering A, 2018, 723: 212−220.

[26] LI J R, XIE D S, ZENG Z R, SONG B, XIE H B, PEI R S, PAN H C, REN Y P, QIN G W. Mechanistic investigation on Ce addition in tuning recrystallization behavior and mechanical property of Mg alloy [J]. Journal of Materials Science & Technology, 2023, 132: 1−17.

[27] LEE D H, LEE G M, PARK S H. Difference in extrusion temperature dependences of microstructure and mechanical properties between extruded AZ61 and AZ91 alloys [J]. Journal of Magnesium and Alloys, 2023, 11: 1683−1696.

[28] NAKATA T, XU C, OHASHI H, YOSHIDA Y, YOSHIDA K, KAMADO S. New Mg−Al based alloy sheet with good room-temperature stretch formability and tensile properties [J]. Scripta Materialia, 2020, 180: 16−22.

[29] JIN S C, CHA J W, BAE J H, YU H, PARK S H. Effects of Al addition on microstructure and mechanical properties of extruded Mg−3Bi alloy [J]. Journal of Magnesium and Alloys, 2022, 10: 1887−1898.

[30] JIANG H S, QIAO X G, ZHENG M Y, WU K, XU C, KAMADO S. The partial substitution of Y with Gd on microstructures and mechanical properties of as-cast and as-extruded Mg−10Zn−6Y−0.5Zr alloy [J]. Materials Characterization, 2018, 135: 96−103.

[31] LUO Lin, CHENG Wei-li, YU Hui, WANG Hong-xia, NIU Xiao-feng, WANG Li-fei, LI Hang, YOU Zhi-yong, HOU Hua. Dynamic recrystallization behavior and strengthening mechanism of quasi-precipitate-free dilute Mg−Bi−Sn alloy [J]. Materials Science and Engineering A, 2022, 850: 143553.

[32] ZHONG Shi-yu, ZHANG Ding-fei, CHAI Sen-sen, ZHOU Jie, HUA Jian-rong, XU Jun-yao, JIANG Bin, PAN Fu-sheng. Effect of Cu addition on the microstructure, mechanical properties and degradation rate of Mg−2Gd alloy [J]. Journal of Materials Research and Technology, 2021, 15: 477−487.

[33] ZHONG Shi-yu, ZHANG Ding-fei, WANG Yong-qin, CHAI Sen-sen, FENG Jing-kai, LUO Yu-lun, HUA Jian-rong, DAI Qi-min, HU Guang-shan, XU Jun-yao, JIANG Bin, PAN Fu-sheng. Microstructures, mechanical properties and degradability of Mg−2Gd−0.5(Cu/Ni) alloys: A comparison study [J]. Journal of Materials Science & Technology, 2022, 128: 44−58.

[34] LIAO Hong-xin, KIM J, LIU Ting-ting, TANG Ai-tao, SHE Jia, PENG Peng, PAN Fu-sheng. Effects of Mn addition on the microstructures, mechanical properties and work-hardening of Mg−1Sn alloy [J]. Materials Science and Engineering A, 2019, 754: 778−785.

[35] SHI Zhi-ming, LIU Ming, ATRENS A. Measurement of the corrosion rate of magnesium alloys using Tafel extrapolation [J]. Corrosion Science, 2010, 52: 579−588.

[36] WANG Nai-guang, WANG Ri-chu, PENG Chao-qun, FENG Yan. Enhancement of the discharge performance of AP65 magnesium alloy anodes by hot extrusion [J]. Corrosion Science, 2014, 81: 85−95.

[37] WANG Qing-hang, ZHAI Hao-wei, LIU Lin-tao, XIA Hong-bo, JIANG Bin, ZHAO Jun, CHEN Dao-lun, PAN Fu-sheng. Novel Mg−Bi−Mn wrought alloys: The effects of extrusion temperature and Mn addition on their microstructures and mechanical properties [J]. Journal of Magnesium and Alloys, 2022, 10: 2588−2606.

[38] LIU Chun-quan, CHEN Xian-hua, CHEN Jiao, ATRENS A, PAN Fu-sheng. The effects of Ca and Mn on the microstructure, texture and mechanical properties of Mg−4Zn alloy [J]. Journal of Magnesium and Alloys, 2022, 9: 1084−1097.

[39] JIN Zhong-zheng, ZHA Min, YU Zhi-yuan, MA Pin-kui, LI Yong-kang, LIU Jin-ming, JIA Hai-long, WANG Hui-yuan.

Exploring the Hall−Petch relation and strengthening mechanism of bimodal-grained Mg−Al−Zn alloys [J]. Journal of Alloys and Compounds, 2020, 833: 155004.
[40] CHENG Wei-li, TIAN Quan-wei, YU Hui, ZHANG Hua, YOU B S. Strengthening mechanisms of indirect-extruded Mg−Sn based alloys at room temperature [J]. Journal of Magnesium and Alloys, 2014, 2: 299−304.
[41] LIU Ming, QIU Dong, ZHAO Ming-chun, SONG Guang-ling, ATRENS A. The effect of crystallographic orientation on the active corrosion of pure magnesium [J]. Scripta Materialia, 2008, 58: 421−424.
[42] LIU Yan-hui, CHENG Wei-li, ZHANG Yao, NIU Xiao-feng, WANG Hong-xia, WANG Li-fei. Microstructure, tensile properties, and corrosion resistance of extruded Mg−1Bi−1Zn alloy: The influence of minor Ca addition [J]. Journal of Alloys and Compounds, 2020, 815: 152414.
[43] YU Xiao-wen, JIANG Bin, YANG Hong, YANG Qing-shan, XIA Xiang-sheng, PAN Fu-sheng. High temperature oxidation behavior of Mg−Y−Sn, Mg−Y, Mg−Sn alloys and its effect on corrosion property [J]. Applied Surface Science, 2015, 353: 1013−1022.
[44] LI Mei-xuan, WANG Cheng, LI Yi-jia, WANG Da-wei, ZHA Min, GAO Yi-peng, WANG Hui-yuan. Tailoring the microstructure and enhancing the corrosion resistance of extruded dilute Mg−0.6Al−0.5Mn−0.25Ca alloy by adding trace Ce [J]. Corrosion Science, 2022, 207: 110605.
[45] CHEN Yu-hang, CHENG Wei-li, GU Xiong-jie, YU Hui, WANG Hong-xia, NIU Xiao-feng, WANG Li-fei, LI Hang. Discharge performance of extruded Mg−Bi binary alloys as anodes for primary Mg-air batteries [J]. Journal of Alloys and Compounds, 2021, 886: 161271.
[46] JIANG Wei-yan, WANG Jing-feng, ZHAO Wei-kang, LIU Qing-shan, JIANG Dian-ming, GUO Sheng-feng. Effect of Sn addition on the mechanical properties and bio-corrosion behavior of cytocompatible Mg−4Zn based alloys [J]. Journal of Magnesium and Alloys, 2019, 7: 15−26.

异质结构低合金化 Mg−1Bi−0.5Sn−0.5In 合金的力学性能和腐蚀行为

徐鸿伟[1]，许文婷[1]，程伟丽[1,2]，李 戬[2]，王利飞[1]，余 晖[3]，王金辉[2]，侯 华[4]，Kwang Seon SHIN[5]

1. 太原理工大学 材料科学与工程学院，太原 030024；
2. 青海大学 盐湖化工研究院开放项目，西宁 810016；
3. 河北工业大学 材料科学与工程学院，天津 300132；
4. 中北大学 材料科学与工程学院，太原 030051；
5. Magnesium Technology Innovation Center, Department of Materials Science and Engineering, Seoul National University, Seoul-08826, Korea

摘 要：通过扫描电子显微镜(SEM)、电子背散射衍射(EBSD)、X 射线光电子能谱(XPS)、电化学测试和拉伸试验，研究了挤压态低合金化 Mg−1Bi−0.5Sn−0.5In (质量分数，%)合金的显微组织特征、腐蚀行为和拉伸性能。结果表明：合金具有由动态再结晶晶粒和变形晶粒组成的异质结构。合金的屈服强度(TYS)、抗拉强度(UTS)和伸长率(EL)分别为 254.8 MPa、315.4 MPa 和 25.3%，表现出良好的强度−韧性协同性。此外，在 3.5% (质量分数) NaCl 溶液中，随着浸泡时间的延长，合金的腐蚀模式由点蚀转变为丝状腐蚀，浸泡 24 h 后，形成复合氧化膜(SnO_2−Bi_2O_3−In_2O_3)，从而延缓腐蚀进程，最终腐蚀速率趋于稳定(P_H=1.53 mm/a)。

关键词：镁合金； 挤压； 腐蚀行为； 拉伸性能； 强化机制

(Edited by Bing YANG)